We are IntechOpen, the world's leading publisher of Open Access books
Built by scientists, for scientists

6,900
Open access books available

186,000
International authors and editors

200M
Downloads

Our authors are among the

154
Countries delivered to

TOP 1%
most cited scientists

12.2%
Contributors from top 500 universities

CLARIVATE ANALYTICS
BOOK CITATION INDEX
INDEXED

WEB OF SCIENCE™

Selection of our books indexed in the Book Citation Index in Web of Science™ Core Collection (BKCI)

Interested in publishing with us?
Contact book.department@intechopen.com

Numbers displayed above are based on latest data collected.
For more information visit www.intechopen.com

9

Surface Acoustic Wave Based Wireless MEMS Actuators for Biomedical Applications

Don W. Dissanayake, Said Al-Sarawi and Derek Abbott
The School of Electrical and Electronic Engineering
The University of Adelaide
Australia. SA 5005

1. Introduction

MEMS technologies have made it possible to fabricate small size, and high performance implantable devices to meet critical medical and biological needs such as site specific *in–vivo* drug delivery, Lab–on–a–Chip (LoC), micro total analysis systems, and polymerase chain reaction (PCR).

Actuators are one of the important components in Bio-MEMS, especially for fluid manipulation. The design of a suitable actuator device to pump the fluid at the microscale, for accurate operation, is of great importance. Many types of microactuators have been developed to match different requirements for various applications (Tsai & Sue, 2007; Varadan & Varadan, 2000). With miniaturisation, physical scaling laws inherently favour some technologies and phenomena over others. In some cases, technologies that can be made by micromachining work well at the microscopic scale, but have no analogy or usefulness in the macroscopic scale. Moreover most of these actuators are too complicated to fabricate within a micropump structure.

Notably, Surface Acoustic Wave (SAW) devices are used to develop micromachines such as ultrasonic micromotors and fluid transfer methodologies such as flexural micropumps (Wixforth, 2003; Strobl et al., 2004). Currently available microfabrication technologies such as photolithography and X–ray lithography with a combination of other processes have enabled the use of SAW devices for a variety of self–contained MEMS applications, which have advanced functionality and performance. The key benefits of these micromachines are; their small size, ease of production, and low–cost. The use of SAWdevices for micro actuation applications provides the great benefit of controlling and interrogation of devices remotely, without direct physical user intervention (Dissanayake et al., 2007; Varadan & Varadan, 2000; Jones et al., 2008).

In this chapter, SAW based novel batteryless and low–powered, secure, and wireless interrogation as well as actuation mechanisms for implantable MEMS devices such as actuators are introduced and investigated. This approach is based on SAW technology and significantly different from currently existing techniques, as the proposed method consists of dual functionality; the secure interrogation and actuation. Consequently such a microactuator can be embedded in a microfluidic device to modulate the fluid flow using less power compared to other mechanisms, such as piezoelectric micropumps. In Section 2, the use of SAW devices for micro actuation is presented and discussed. Section 3 explains

Source: Acoustic Waves, Book edited by: Don W. Dissanayake,
ISBN 978-953-307-111-4, pp. 466, September 2010, Sciyo, Croatia, downloaded from SCIYO.COM

the operation of the SAW device based microactuator. The underlying theoretical model is then elaborated in Section 4 and followed by Section 5, which presents a method to derive the electric potential for electrostatic actuation. Section 6 shows a theoretical boundary condition analysis for the proposed model. Section 7 presents detailed Finite Element Modelling (FEM) of the actuator. Then simulation results are discussed in Section 8, and followed by the conclusion in Section 9.

2. SAW device based microactuator

SAW devices are widely used in MEMS applications, which require secure, wireless, and passive interrogation Jones et al. (2008). These devices are recognised for their versatility and efficiency in controlling and processing electrical signals. They are based on propagation of acoustic waves in elastic solids and the coupling of these waves to electric charge signals via an input and an output Inter Digital Transducers (IDT) that are deposited on the piezoelectric substrate. As shown in Figure 1, a SAW device consisting of a solid substrate with input and output IDTs Jones et al. (2008). An IDT is an array of narrow and parallel electrodes connected alternately to two bus bars made out of thin–film metal. The purpose of placing a set of IDTs on a SAW device is to provide a coupling between the electrical signal received (or transmitted) and the mechanical actuation of the piezoelectric substrate material. Since SAW devices are mostly used for wireless applications, a micro–antenna is need to be attached to the input IDT.

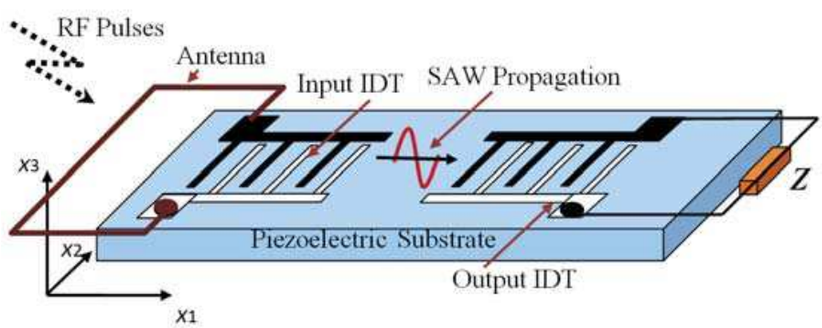

Fig. 1. Standard SAW device consist of a piezoelectric substrate, input IDT, and an output IDT. Input IDT is connected to a micro-antenna for wireless communication, and a load is connected to the output IDT for measurements.

Acoustic waves in these devices are propagating as surface waves, and hence can be perturbed easily by modifications to the substrate surface. Such features have enabled a large number of resonant sensors for applications such as chemical sensors Ruppel et al. (2002), gyroscopes Varadan & Varadan (2000), and accelerometers Subramanian et al. (1997). SAW devices also find application in oscillators, pulse compressors, convolvers, correlators, multiplexers and demultiplexers Ruppel et al. (2002).

SAW device related technology has been utilised to design and develop MEMS based microaccelerometers and gyroscopes for military and similar applications (Varadan & Varadan, 2000; Subramanian et al., 1997). The technology used in those applications is similar to the capacitor effect generated by programmable tapped delay lines, which use the principle of air gap coupling (Milstein & Das, 1979) between the SAW substrate and a silicon superstrate; a silicon layer superimposed on the SAW device. These capacitors are then used

to control the amount of RF coupling from the input IDT on the SAW substrate to the output terminal on the silicon chip (Subramanian et al., 1997). It is a well known method to use a sandwich structure of semiconductor on piezoelectric substrate to form the so called space–charge coupled SAW devices and SAW convolvers (Milstein & Das, 1979).
Such an approach can be utilised in the design of a SAW based microactuator. The proposed approach for the actuator design is converse to the method used by Varadan et. Al (Subramanian et al., 1997) for the microaccelerometer design. Being an elastic deformation wave on a piezoelectric substrate, the SAW induces charge separation. Thus it carries an electric field with it, which exists both inside and outside the piezoelectric substrate and decays according to Laplace's equation. In this SAW device based actuator, a thin conductive plate is placed on top of the output IDT, which is separated by an air–gap. The conductive plate does not alter the mechanical boundary conditions of the SAW substrate, but causes the surface to be equipotential and the propagating electric potential to be zero at the surface of the conductive plate. As a result, an electrostatic force is generated between the conductive plate and the output IDT in the SAW device causing micro deformations in the conductive plate.

3. Proposed microactuator operation

Figure 2 depicts the wireless interrogation unit for the SAW based microactuator. The actuator is made of a conductive material or alternatively, it can be made of a material such as Silicon (Si) or Silicon Nitride (Si_3N_4) and the bottom surface of the microactuator can be coated with a thin conductive material such as Gold, Platinum or Aluminium. The SAW substrate is made out of 128-YX-Lithium Niobate ($LiNbO_3$), as it is best suited for Rayleigh wave propagation.

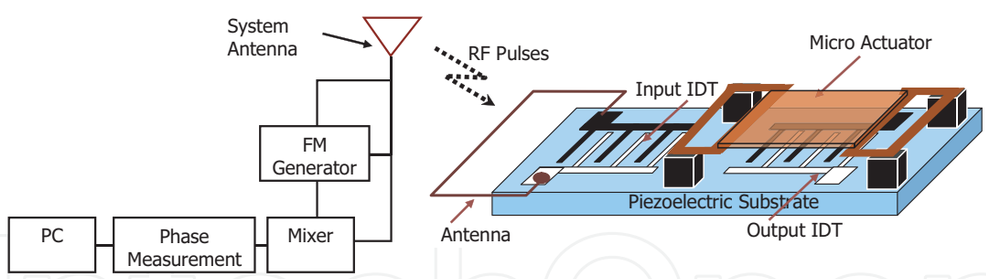

Fig. 2. Wireless interrogation unit for SAW device based actuator. The microactuator is placed on top of the output IDT of a SAW device. SAW device consists of a piezoelectric substrate, input IDT, and output IDT. Input IDT is connected to a micro-antenna for wireless interrogation.

Effectively, the output IDT and the conductive plate are used to generate an air–gap coupled SAW based electrostatic actuator. The device operation is as follows. The input IDT generates Rayleigh waves using inverse piezoelectric effect based on the RF signal that is being fed to the SAW device through the microstrip antenna. The Output IDT regenerates the electric signal using the piezoelectric effect of the SAW device. As it was explained in Section 2, the generated electrostatic field between this propagating electric potential wave and the conductive plate on top of the output IDT creates a compulsive and repulsive force between the two. Since the conductive plate is a thin flexural plate, it bends as a function of the applied electrostatic field enabling its use as a microactuator.

4. Theoretical analysis of the electrostatic actuation

In this section, a detailed theoretical analysis is carried out to analyse the generated electrostatic force at the conductive actuator. In achieving this, first the behavior of the propagating SAW on piezoelectric media is analysed. Then the analysis is focused towards deriving a general expression for the electric potential regenerated at the output IDT of the SAW device. Additionally, a boundary condition analysis is also presented, considering a specific scenario; the placement of the conductive actuator on top of the output IDT as shown in Figure 3.

4.1 Problem description

A variety of approaches have been followed by other researchers to investigate the SAW propagation in different piezoelectric substrates. These include, but not limited to, Potassium Niobate ($KNbO_3$), Lithium Tantalate ($LiTaO_3$), Lead Potassium Niobate ($Pb_2KNb_5O_{15}$ or PKN) (Dvoesherstov et al., 2000; Dvoesherstov & Chirimanov, 1999), and various cuts in Lithium Niobate $LiNbO_3$ (Gardner et al., 2001). However, the requirement of a detailed analysis of the use of 128-XY $LiNbO_3$, specific to the novel SAWbased actuator is of great importance. Therefore a descriptive theoretical analysis was carried out and presented in following sections.

In a SAW device, IDT patterns can be considered as a periodic structure. When an acoustic wave propagates on the surface through the periodic structure, it is partially reflected at each IDT finger. Depending on the operating frequency of the acoustic wave, the reflected parts interfere constructively or destructively (Zaglmayr et al., 2005). Generally, these reflections are considered to be very small and therefore, in this analysis the effect of the reflections is discarded and it is assumed that a surface wave propagate through each IDT finger only once. As can be seen from Figure 3, the direction of periodicity is denoted by x_1, the surface normal direction by x_3, and their perpendicular direction by x_2 following a *right-handed* coordinate system. The dimensional extension of electrodes in x_2 direction (length of the IDT fingers) is much larger in comparison to the periodicity. Additionally, a homogenous material topology is assumed in x_2 direction for this analysis.

4.2 Rayleigh waves

In general, SAWs consist of different types of propagation modes that are considered to be 3D. It is highly important to choose a suitable propagation mode for the SAW device especially when it is designed for microfluidic applications. Therefore, different acoustic modes need to be analysed. For example, one would expect horizontal shear SAW mode to be more useful than Rayleigh SAW mode. This is because when a SAW device is in vitro, Rayleigh SAW mode is rapidly damped out, due to the pressure generated by the surrounding fluid (Jones et al., 2008). In contrast to the general approach of using the SAW device surface to transfer the fluid, the proposed approach uses an actuator (conductive plate), which is on top of the SAW substrate. As a result the fluid flow is isolated from the SAW substrate and hence it prohibits the interaction of the fluid with the SAW mode. Moreover, Rayleigh SAW mode is best suited for space-charge related applications as most of the energy in this mode is concentrated within one wavelength of the substrate (Milstein & Das, 1979), as shown in Figure 4. Hence, considering the measures taken to isolate the SAW substrate from the fluid in this approach, Rayleigh SAW mode was chosen.

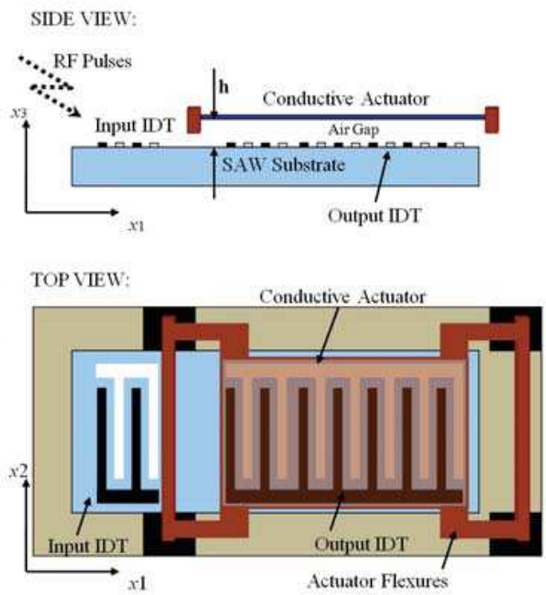

Fig. 3. A concept drawing of the SAW actuator model. Side view: Air–gap separated conductive actuator is placed above the output IDT of the SAW device (not to scale). Top view: The actuator consists of flexures to reduce the spring constant. SAW substrate is a rotated crystal cut to make sure the wave propagation in x_1 direction and h is the height of the air gap.

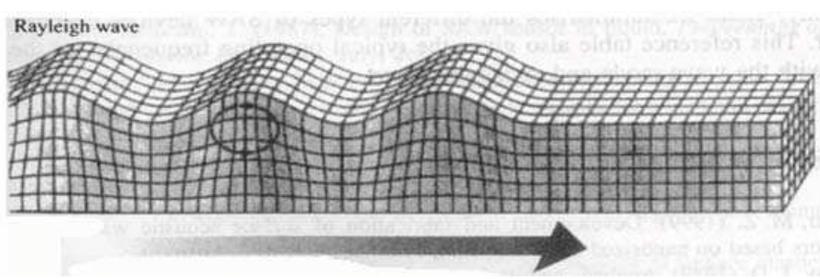

Fig. 4. Rayleigh Wave Mode which shows elliptical particle displacements (Gardner et al., 2001).

Rayleigh waves propagates near the surface of the piezoelectric substrate, the amplitude decreases rapidly within depth in x_3 direction, and becomes negligibly small within the depth of a few wavelengths from the surface (Zaglmayr et al., 2005). This behaviour is further elaborated and mathematically represented in coming sections.

The orientation of the piezoelectric material affects the SAW propagation on the substrate. Therefore, a certain crystal cut is required to direct the surface wave towards a desired direction. Here for this analysis, 128-XY $LiNbO_3$ is chosen as the substrate material due to its high electromechanical coupling coefficient (Čiplys & Rimeika, 1999; Gardner et al., 2001). This orientation facilitate the Rayleigh mode to propagate in x_1 direction and contained in a sagittal plane define by x_1–x_3 plane. Therefore, instead of performing a full three-dimensional analysis, a model reduction is performed in the geometric domain and the analysis is carried out within the sagittal plane.

In order to derive an expression for the resultant electrostatic force, the following assumptions are made of the model and the analysis, as well as simplifications to both are mentioned. In piezoelectric materials, the frequency of the induced electric field wave is sufficiently small enough to reasonably assume the electromagnetic coupling effects to be negligible. This means that local perturbations are felt almost instantaneously through out the substrate (Gantner et al., 2007; Kannan, 2006; Maugin, 1985).

Additionally, if l is the largest characteristic dimension of the actuator structure and c is the speed of light, the generated electromagnetic coupling effects can be safely discarded, if the operating frequency of the device is much less than the ratio c/l (Zaglmayr et al., 2005; Horenstein et al., 2000). Here, for $l \sim 3$ mm, $c/l \approx 100$ GHz. Therefore, since the chosen signal frequency of SAW is in the range of 50 – 100 MHz ($\ll c/l$), electromagnetic coupling effects can be safely discarded, and hence the electric field can be treated as quasi–static.

4.3 Piezoelectric equations

In piezoelectric analysis, quasi–static electric field is achieved by setting the permeability to zero, corresponding to an infinite speed of the electromagnetic wave. Using Maxwell's equations, electromagnetic quasi–static approximation can be written as

$$E_i = -\frac{\partial \Phi}{\partial x_i}, \tag{1}$$

$$\nabla \cdot D = 0, \tag{2}$$

where E is the electric field intensity, Φ is the electric potential, D is the electric flux density (dielectric displacement) and x_i (for i = 1, 2, 3) shows the direction of interest as shown in Figure 3. Here, Equation 2 elaborate the fact that piezoelectric materials are insulators hence there are no free volume charges (Zaglmayr et al., 2005). Moreover, from the mechanical equations of motion, the relationship between the mechanical displacement u, and the mechanical stress T is given by

$$\rho \frac{\partial^2 u_i}{\partial t^2} = \sum_j \frac{\partial T_{ij}}{\partial x_i}, \tag{3}$$

where ρ is the density of the piezoelectric substrate. For a piezoelectric media, the relation between the mechanical strain S and mechanical displacement u can be written as

$$S_{ij} = \frac{1}{2}\left[\frac{\partial u_i}{\partial x_j} + \frac{\partial u_j}{\partial x_i}\right]. \tag{4}$$

In order to investigate the behaviour of the electric potential and the mechanical displacement of SAW, the constitutive equations for piezoelectric material are also need to be considered. The constitutive equations for piezoelectric material can be obtained by extending Hook's law and the electrostatic equation for the electric flux density. Therefore, the relationship between D, E, T and S in a SAW substrate can be written as

$$T_{ij} = \sum_k \sum_l c_{ijkl}^E S_{kl} - \sum_k e_{kij} E_k, \tag{5}$$

$$D_i = \sum_j \sum_k e_{ijk} S_{jk} + \sum_j \varepsilon_{ij}^S E_j, \tag{6}$$

where c_{ijkl} is the stiffness tensor for constant electric field, e_{ijk} is the piezoelectric coupling tensor (e_{kij} is the corresponding transpose tensor of e_{ijk}), ε_{ij} is the permittivity tensor for constant strain and i, j, k, l vary from 1 to 3. It should be noted that the mechanical stiffness matrix [$\boldsymbol{c}$] and the permittivity matrix [$\boldsymbol{\varepsilon}$] are symmetric. Additionally, the direct and converse piezoelectric effects are also symmetric, hence in piezoelectric matrix [$\boldsymbol{e}$], the coupling coefficients are equal for both the effects (Zaglmayr et al., 2005). These symmetry considerations allow the reduction of the corresponding matrices of the material tensors; [$\boldsymbol{c}$] to a 6×6 symmetric matrix, [$\boldsymbol{\varepsilon}$] to a 3×3 symmetric matrix, and [$\boldsymbol{e}$] to a 6×3 matrix.
Equations 1– 6 lead to a system of four coupled equations, which are represented by Equations 7 and 8.

$$\sum_j \sum_k \left[e_{kij} \frac{\partial^2 \Phi}{\partial x_j \partial x_k} + \sum_l c_{ijkl}^E \frac{\partial^2 u_k}{\partial x_j \partial x_l} \right] = \rho \frac{\partial^2 u_i}{\partial t^2}, \tag{7}$$

$$\sum_i \sum_j \left[\varepsilon_{ij}^S \frac{\partial^2 \Phi}{\partial x_i \partial x_j} - \sum_k e_{ijk} \frac{\partial^2 u_j}{\partial x_i \partial x_k} \right] = 0. \tag{8}$$

This relationship between mechanical displacement and electric potential is considered in a semi–infinite, isotropic and homogenous linear elastic space as shown in Figure 4. As was mentioned above, the piezoelectric crystal cut ensures the Rayleigh wave propagate in the x_1-x_3 sagittal plane as shown in Figure 3. An alternative definition to the sagittal plane, can be given as, the plane defined by the real wave vector (wave number) k and the unit vector normal to the surface of the SAW substrate (x_3 direction).
Various approaches have been proposed by researchers to solve wave propagation on anisotropic substrates (Zaglmayr et al., 2005; Gantner et al., 2007; Adler, 2000). The method of partial waves is considered to be a commonly used technique to analyse different SAW modes on anisotropic substrates such as piezoelectrics. Therefore, in this research the method of partial waves is used to solve this wave propagation phenomena for the SAW actuator model. As a result, plane wave solutions of the form given in Equations 9 and 10 are considered for the mathematical modelling of this device,

$$u_j^m(x_1, x_3, t) = \alpha_j^m e^{\mathrm{i}kb^m x_3} e^{\mathrm{i}k(x_1 - vt)}, \tag{9}$$

$$\Phi^m(x_1, x_3, t) = \alpha_4^m e^{\mathrm{i}kb^m x_3} e^{\mathrm{i}k(x_1 - vt)}, \tag{10}$$

where the α_j^m values are linear coefficients that depend on the decaying constant b_m is the phase velocity of the wave, k (= $2\pi/\lambda$) is the wave vector, λ is the wavelength, i is the standard imaginary unit (= $\sqrt{-1}$), m = 1, 2, 3, 4 and j = 1, 2, 3.
Equations 7 and 8, a linear system for the coefficients α_j^m can be obtained and solved. In solving these equations, it is necessary to transform the material parameters of the SAW substrate to match the coordinate system of the problem. This is discussed in Section 4.4.

4.4 Transformation of coordinates

As it was mentioned above, different crystal cuts consist of different material properties. Therefore it is significant to consider the specific orientation of the selected crystal for a specific analysis, to obtained the desired SAW mode. In the equations of motion the material parameters are expressed in terms of structural coordinate axes that are selected for convenient boundary condition and excitation requirements. However, the material parameters are presented in the form of [$\boldsymbol{c}$], [$\boldsymbol{\varepsilon}$], and [$\boldsymbol{e}$] matrices as was mentioned in Section 4.3, and these are expressed according to the crystalline axes. Therefore it is necessary to transform the material parameters to match the coordinate system of the problem. Generally, the parameters are transformed using a transformation matrix [$\boldsymbol{r}$] given by

$$[\boldsymbol{r}]=\begin{bmatrix} \cos\psi.\cos\phi. & \cos\psi\sin\phi. & \sin\psi\sin\theta \\ -\cos\theta\sin\phi\sin\psi & +\cos\theta\cos\phi\sin\psi & \\ \sin\psi.\cos\theta & -\sin\psi\sin\phi & \cos\psi\sin\theta \\ -\cos\theta\sin\phi\cos\psi & +\cos\theta\cos\phi\cos\psi & \\ \sin\theta\sin\phi & -\sin\theta\cos\phi & \cos\theta \end{bmatrix}=\begin{bmatrix} r_{11} & r_{12} & r_{13} \\ r_{21} & r_{22} & r_{23} \\ r_{31} & r_{32} & r_{33} \end{bmatrix},$$

where the elements of this matrix are the direction cosines between the crystalline axis and the problem axis (Subramanian et al., 1997; Kannan, 2006; Wolfram MathWorld, 2009).
In this research, the X–convention is followed for specifying the order of rotation of the axes. The rotations specified by the Euler angle set that are related to the X-convention and the rotation order are explained in Figure 5.

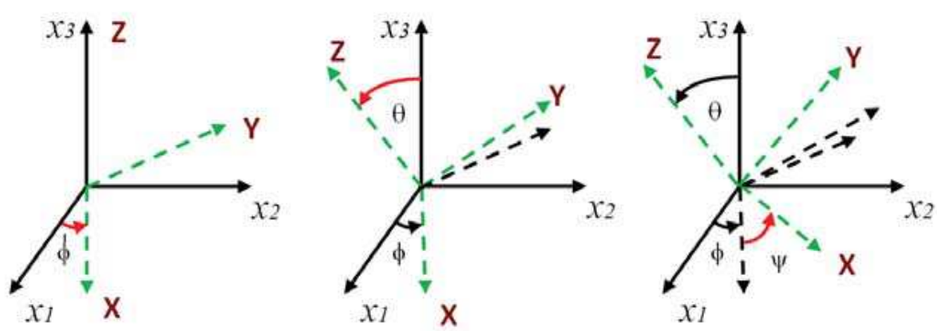

Fig. 5. Transformation of coordinate system. Transformation of coordinate system using **X**–convention. Here $x_1x_2x_3$ is the structural coordinate system and XYZ is the crystal coordinate system. Here x_1 determines the wave propagation direction and x_3 is normal to the crystal surface. Initially both of these axes are parallel to each other. While the structural coordinate axes always remain same, the crystal axes XYZ are rotated by an angle ϕ around Z axis, then by an angle θ around X axis and finally by an angle ψ once again around Z axis. The direction cosines are then derived based on the Euler angles.

Once the transformation matrix is defined, the matrices that define the crystal properties ([$\boldsymbol{c}$], [$\boldsymbol{\varepsilon}$], and [$\boldsymbol{e}$]) are then transformed using the Bond–Transformation procedure (Upadhyay, 2004). The advantage associated with the this procedure, for stiffness and

compliance, is that Bond-Transformation is directly applied on stiffness or compliance constants given in *abbreviated subscript notation*. Therefore the transformation laws of this procedure can be shown as

$$[\boldsymbol{c}_r] = [\boldsymbol{M_B}][\boldsymbol{c}][\boldsymbol{M}_B^T], \tag{11}$$

$$[\boldsymbol{e}_r] = [\boldsymbol{M_B}][\boldsymbol{e}][\boldsymbol{r}^T], \tag{12}$$

$$[\varepsilon_r] = [\boldsymbol{r}][\varepsilon][\boldsymbol{r}^T], \tag{13}$$

where $[\boldsymbol{M}_B]$ is the Bond–Transformation matrix given by

$$[\boldsymbol{M_B}] = \begin{bmatrix} r_{11}^2 & r_{12}^2 & r_{13}^2 & 2r_{12}r_{13} & 2r_{11}r_{13} & 2r_{11}r_{12} \\ r_{21}^2 & r_{22}^2 & r_{23}^2 & 2r_{22}r_{23} & 2r_{21}r_{23} & 2r_{21}r_{22} \\ r_{31}^2 & r_{32}^2 & r_{33}^2 & 2r_{32}r_{33} & 2r_{31}r_{33} & 2r_{31}r_{32} \\ r_{21}r_{31} & r_{22}r_{32} & r_{23}r_{33} & r_{22}r_{33}+r_{32}r_{23} & r_{21}r_{33}+r_{31}r_{23} & r_{21}r_{32}+r_{31}r_{22} \\ r_{11}r_{31} & r_{12}r_{32} & r_{13}r_{33} & r_{12}r_{33}+r_{32}r_{13} & r_{31}r_{13}+r_{11}r_{33} & r_{11}r_{32}+r_{31}r_{12} \\ r_{11}r_{21} & r_{12}r_{22} & r_{13}r_{23} & r_{12}r_{23}+r_{22}r_{13} & r_{11}r_{23}+r_{21}r_{13} & r_{11}r_{22}+r_{21}r_{12} \end{bmatrix}.$$

$[\boldsymbol{r}_T]$ denotes the transpose of the matrix $[\boldsymbol{r}]$. $[\boldsymbol{c}_r]$ is the transformed stiffness matrix, $[\boldsymbol{e}_r]$ is the transformed piezoelectric matrix and $[\boldsymbol{\varepsilon}_r]$ is the transformed permittivity matrix. These transformed matrices can be used to derive more specific partial wave equations for a certain SAW mode for a known crystal cut as shown in the following section.

4.5 Calculations for lithium niobate crystals

It is highly important to select a piezoelectric material with high electromechanical coupling in order to maximise the signal strength of the electric potential at the output IDT of the SAW device. Therefore, 128-YX-$LiNbO_3$ is chosen for this device, as it consists of the highest electromechanical coupling efficiency for Rayleigh SAW modes, compared to other commonly used piezoelectric substrates (Čiplys & Rimeika, 1999). Following the crystal transformation procedure described in Section 4.4, the coordinations of substrate is need to be transformed into a coordinate system defined by x_1, x_2 and x_3 as shown in Figure 3. This results in a new set of material parameters for the substrate, which is then used during the derivation of electric potential and mechanical displacement functions of the SAW mode.
The Euler angles associated with the crystal rotation for 128-YX-$LiNbO_3$ is (0,38°,0), and the rotated material parameters take the general form as presented below.

$$[\boldsymbol{c}_r] = \begin{bmatrix} c_{11} & c_{12} & c_{13} & c_{14} & 0 & 0 \\ c_{12} & c_{22} & c_{23} & c_{24} & 0 & 0 \\ c_{13} & c_{23} & c_{33} & c_{34} & 0 & 0 \\ c_{14} & c_{24} & c_{34} & c_{44} & 0 & 0 \\ 0 & 0 & 0 & 0 & c_{55} & c_{56} \\ 0 & 0 & 0 & 0 & c_{56} & c_{66} \end{bmatrix}, \ [\boldsymbol{e}_r] = \begin{bmatrix} 0 & e_{12} & e_{13} \\ 0 & e_{22} & e_{23} \\ 0 & e_{32} & e_{33} \\ 0 & e_{42} & e_{43} \\ e_{51} & 0 & 0 \\ e_{61} & 0 & 0 \end{bmatrix}, \ [\varepsilon_r] = \begin{bmatrix} \varepsilon_{11} & 0 & 0 \\ 0 & \varepsilon_{22} & \varepsilon_{23} \\ 0 & \varepsilon_{23} & \varepsilon_{33} \end{bmatrix}$$

In order to derive the specific plane wave equations for this crystal, partial wave Equations 9 and 10 are substituted into the Equations 7 and 8 with the rotated material parameters. As a result, the following Eigenvalue problem can be obtained.

$$\mathbf{M} \cdot \boldsymbol{\alpha} = 0. \tag{14}$$

Alternatively the above equation can be written as,

$$\begin{bmatrix} m_{11} - \rho v^2 & m_{12} & m_{13} & m_{14} \\ m_{12} & m_{22} - \rho v^2 & m_{23} & m_{24} \\ m_{13} & m_{23} & m_{33} - \rho v^2 & m_{34} \\ m_{14} & m_{24} & m_{34} & m_{44} - \rho v^2 \end{bmatrix} \begin{bmatrix} \alpha_1 \\ \alpha_2 \\ \alpha_3 \\ \alpha_4 \end{bmatrix} = 0. \tag{15}$$

The matrix coefficients in Equation 15 are shown below. It should be noted that for a 128-YXLiNbO$_3$ crystal c_{15}, c_{16}, c_{35}, c_{36}, c_{45}, and $c_{46} = 0$. Additionally, e_{11}, e_{31}, e_{41}, e_{53}, e_{63} and $\varepsilon_{13} = 0$. Therefore as shown below, the matrix coefficients in **M** become simpler and the Eigenvalue problem expressed in Equation 15 becomes easier to solve.

$$\begin{aligned}
m_{11} &= c_{55}b^2 + 2c_{15}b + c_{11} &&\Rightarrow\quad m_{11} = c_{55}b^2 + c_{11} \\
m_{12} &= c_{45}b^2 + (c_{14} + c_{56})b + c_{16} &&\Rightarrow\quad m_{12} = (c_{14} + c_{56})b \\
m_{13} &= c_{35}b^2 + (c_{13} + c_{55})b + c_{15} &&\Rightarrow\quad m_{13} = (c_{13} + c_{55})b \\
m_{14} &= e_{53}b^2 + (e_{51} + e_{13})b + e_{11} &&\Rightarrow\quad m_{14} = (e_{51} + e_{13})b \\
m_{22} &= c_{44}b^2 + 2c_{46}b + c_{66} &&\Rightarrow\quad m_{22} = c_{44}b^2 + c_{66} \\
m_{23} &= c_{34}b^2 + (c_{36} + c_{45})b + c_{56} &&\Rightarrow\quad m_{23} = c_{34}b^2 + c_{56} \\
m_{24} &= e_{43}b^2 + (e_{41} + e_{63})b + e_{61} &&\Rightarrow\quad m_{24} = e_{43}b^2 + e_{61} \\
m_{33} &= c_{33}b^2 + 2c_{35}b + c_{55} &&\Rightarrow\quad m_{33} = c_{33}b^2 + c_{55} \\
m_{34} &= e_{33}b^2 + (e_{31} + e_{53})b + e_{51} &&\Rightarrow\quad m_{34} = e_{33}b^2 + e_{51} \\
m_{44} &= -(\varepsilon_{33}b^2 + 2\varepsilon_{13}b + \varepsilon_{11}) &&\Rightarrow\quad m_{44} = -(\varepsilon_{33}b^2 + \varepsilon_{11})
\end{aligned}$$

In order to evaluate the non–trivial solution for Equation 15, the Eigenvalue problem, *det* (**M**) = 0, is required to be solved. This results in a system of characteristic equations for displacement amplitudes and electric potential in which the phase velocity v of the wave is used as unknown parameters. In general case, this system of characteristic equations is reduced to an eighth order polynomial in the decaying constant b for a given value of phase velocity. However, the resulting roots of b are either purely real or complex conjugate pairs. Since these roots leads to Rayleigh waves that decay with the depth along x_3, only the roots with negative imaginary parts are accepted to be consistent with the physical meaning of wave propagation in piezoelectric media (Gardner et al., 2001; Ippolito et al., 2002). There are four such roots for b (denoted as b_m for m = 1, 2, 3, 4) and for each such value, there exist a unique Eigenvector $\boldsymbol{\alpha}^m$. A general solutions is then obtained as a linear combination of partial waves such that each wave decays almost to zero as it shifts into the crystal depth approximately at a distance of several wavelengths from the surface (x_3 = 0). Furthermore, the solution consists of three displacement components u_j (j = 1, 2,3) and the electric potential Φ as described by the Equations 16 and 17.

$$u_j(x_1, x_3, t) = \left[\sum_m C_m \alpha_j^m e^{ikb^m x_3} \right] e^{ik(x_1 - vt)}, \tag{16}$$

$$\Phi(x_1, x_3, t) = \left[\sum_m C_m \alpha_4^m e^{ikb^m x_3} \right] e^{ik(x_1 - vt)}. \tag{17}$$

Additionally, during the derivation of the solution in the form of a SAW, it is assumed that the wave vector k is always parallel to the free surface, while the constant–phase surfaces are always normal to the free surface. Furthermore, it is considered that the multiplier in Equations 16 and 17, which depends on the x_3 coordinate, determines the displacement amplitude, and the wave properties of the solution are determined by the multiplier $e^{ik(x_1 - vt)}$. The weighting coefficients C_m of these plane waves are chosen to satisfy the mechanical and electrical boundary conditions at the surface of the piezoelectric substrate specific to this SAW based actuator model, which is discussed in detail in Section 6. But first, in Section 5, an expression is derived for the electric potential at the output IDT, using Equation 17.

5. Electric potential at output IDT

In order to determine the electrostatic field generated between the output IDT and the conductive plate, the evaluation of the electric potential at the output IDT is required. Here, once the plane wave equation is evaluated for the electric potential wave in the SAW device (Equation 17), an analysis is carried out to evaluate an expression for the electric potential at the output IDT. In achieving this, the following assumptions and simplification are made to the design apart from previously mentioned simplifications.

i. The crystal cut is best set so that the SAW is directly propagating in the x_1 direction to allow an orthogonal interaction between the SAW and the output IDT.
ii. The orientation of the IDT is such that a SAW is generated in the direction of maximum SAW–propagation speed.
iii. The acoustic wave is assumed to pass the output IDT once, and interact with no reflections caused by impedance mismatches (Gardner et al., 2001; Ippolito et al., 2002).
iv. The acoustic wave interact with the IDT in the near field where SAW can be treated as a travelling wave as was discussed before.

Due to the periodic nature of the propagating waves and the placement of the IDTs, the analysis is initially carried out only for a single period, and then extended to the whole structure. The single period placement of the output IDT is shown in Figure 6.

As explained in Figure 6, each finger in the IDT is assigned a negative or positive value that is determined by the finger's connection to either positive or negative bus bar. Therefore, the output IDT fingers are represented as square waves with the period defining wave length of the SAW and the duty cycle defining the finger width (Skinner et al., 2006). This width is $\frac{\lambda}{4}$ for a metallisation ratio of 0.5. For the SAW based electrostatic actuator model, initially a basic model of the IDT configuration is used.

While the output IDT is considered as a combination of square waves, the SAW is defined as a propagating plane wave as was elaborated in Section 4.5. In order to obtain the time response of the SAW interaction with the output IDT, a cross–correlation is applied to the

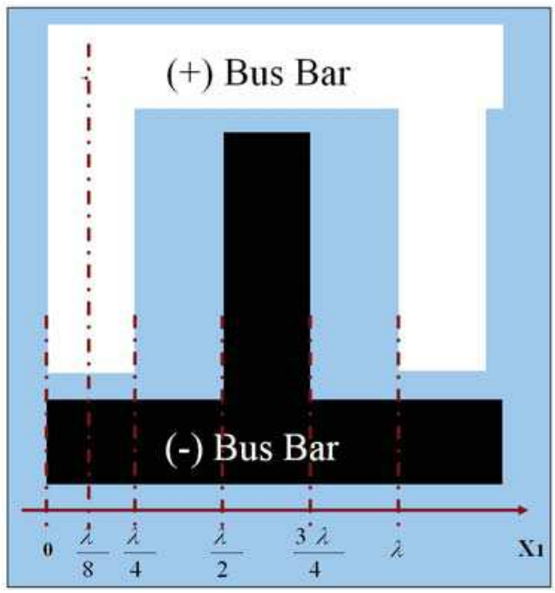

Fig. 6. Periodic IDT finger representation. IDT finger representation for one wavelength (λ) with a metalisation ratio of $\frac{1}{2}$. Each finger is connected to one of the two bus bars, with one bus bar assigned a positive value and the other assigned a negative value.

SAW and the IDT signals. Cross–correlation is a method by which two different function are compared over time with one time–fixed function and one time–shifted function. Within one wavelength of the IDT, the analysis has to be carried out in two parts, considering the space above the output IDT fingers ($0 \le x_1 \le \frac{\lambda}{4} \cup \frac{\lambda}{2} \le x_1 \le \frac{3\lambda}{4}$) and the space above the output IDT gap between fingers ($\frac{\lambda}{4} < x_1 < \frac{\lambda}{2} \cup \frac{3\lambda}{4} < x_1 < \lambda$). This is because the metal based IDT fingers consist of an equipotential distribution for a given time, and the gaps between the fingers consist of a space varying electric potential distribution in x_1 direction.

IDT Segment in Range ($0 \le x_1 \le \frac{\lambda}{4} \cup \frac{\lambda}{2} \le x_1 \le \frac{3\lambda}{4}$ **)**:

As shown in Figure 7, analysis of a single IDT finger will serve as the basis for the analysis for a single periodic structure and then for the entire IDT structure. Therefore, the cross-correlation between the SAW potential signal $\Phi(x_1, x_3, t)$, and the first finger connected to the positive bus bar ($0 \le x_1 \le \frac{\lambda}{4}$) can be expressed as

$$\begin{aligned} C_+(x_1, x_3, t) &= (\Phi * g_{(+)})(x_1, x_3, t) \\ &= \int_0^{T/4} \Phi(x_1, x_3, t+\tau) \cdot g_{(+)}(\tau) d\tau \\ &= \frac{\sqrt{2}}{kv} \Phi(x_1 - \frac{\lambda}{8}, x_3, t). \end{aligned} \tag{18}$$

Here, $g_{(+)}$ represents the positive square wave of the finger as can be seen from Figure 7.

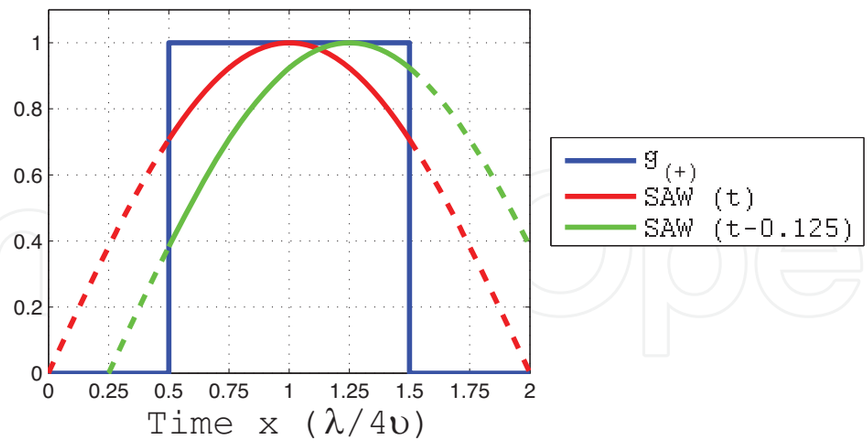

Fig. 7. SAW and single finger correlation. Superimposition of the SAW and a single finger of the output IDT. $g_{(+)}$ represents the equipotential behaviour of the conductive finger. Two SAWs are $T/8$ apart from one another.

The electric potential at this IDT finger can be considered as the average value of the correlated signal $C_+(x_1, x_3, t)$ over the finger width f_w, due to the equipotential nature of the metal based fingers. As the metalisation ratio is 0.5 in this analysis, $f_w = \lambda/4$ and this relate to $T/4$ in time scale, where T (= λ/v) is the time period of the SAW. Therefore, the electric potential generated at the first finger connected to the positive bus bar can be written as

$$\begin{aligned} V_+(x_1,x_3,t) &= \int_0^{\lambda/4} C_+(x_1,x_3,t)dx_1 \\ &= \frac{2T}{\pi^2}\Phi(\frac{\lambda}{8},x_3,t). \end{aligned} \tag{19}$$

By following an identical approach, the electric potential at the finger connected to the negative bus bar ($\frac{\lambda}{2} \le x_1 \le \frac{3\lambda}{4}$) can be derived and the result can be written as

$$V_-(x_1,x_3,t) = -\frac{2T}{\pi^2}\Phi(\frac{\lambda}{8},x_3,t). \tag{20}$$

IDT Segment in Range ($\frac{\lambda}{4} < x_1 < \frac{\lambda}{2} \cup \frac{3\lambda}{4} < x_1 < \lambda$):

Once the analysis is simplified by considering the aforementioned assumptions and simplifications, the electric potential at the gaps between the fingers can be considered to consist of the same electric potential of the propagating SAW as shown in Equation 17. Therefore

$$V_{gap}(x_1,x_3,t) = \Phi(x_1,x_3,t). \tag{21}$$

Based on the above analysis, the total electric potential generated by a single period of the output IDT can be expressed as

$$\Phi(x_1,x_3,t)=\begin{cases}\Psi, & for\ \ 0\le x_1\le \frac{\lambda}{4}\\ \Omega, & for\ \ \frac{\lambda}{4}<x_1<\frac{\lambda}{2}\\ -\Psi, & for\ \ \frac{\lambda}{2}\le x_1\le \frac{3\lambda}{4}\\ -\Omega, & for\ \ \frac{3\lambda}{4}<x_1<\lambda\end{cases}, \tag{22}$$

where $\Psi = V_+(x_1, x_3, t) = \frac{2T}{\pi^2}\,\Phi(\frac{\lambda}{8}, x_3, t)$, and $\Omega = V_{gap}(x_1, x_3, t) = \Phi(x_1, x_3, t)$. This is further elaborated graphically in Figure 8. Consequently, due to the periodic nature of the IDT, this expression can be easily extended to derive the electric potential for the full output IDT. Therefore, for an output IDT with N_p finger pairs, the total electrostatic potential at the output IDT can be expressed as

$$\Phi(x_1,x_3,t)=\begin{cases}\Psi, & for\ \ n\lambda\le x_1\le (\frac{1}{4}+n)\lambda\\ \Omega, & for\ \ (\frac{1}{4}+n)\lambda<x_1<(\frac{1}{2}+n)\lambda\\ -\Psi, & for\ \ (\frac{1}{2}+n)\lambda\le x_1\le (\frac{3}{4}+n)\lambda\\ -\Omega, & for\ \ (\frac{3}{4}+n)\lambda<x_1<(1+n)\lambda\end{cases}. \tag{23}$$

Here, $n = 0, 1, 2, \ldots, (N_p - 1)$ and Ψ and Ω are as explained before.
Once the general expressions is derived, a boundary condition analysis is carried out to specify values for the weighting coefficients in Equations 22 and 23. This analysis is further unfolded in next section.

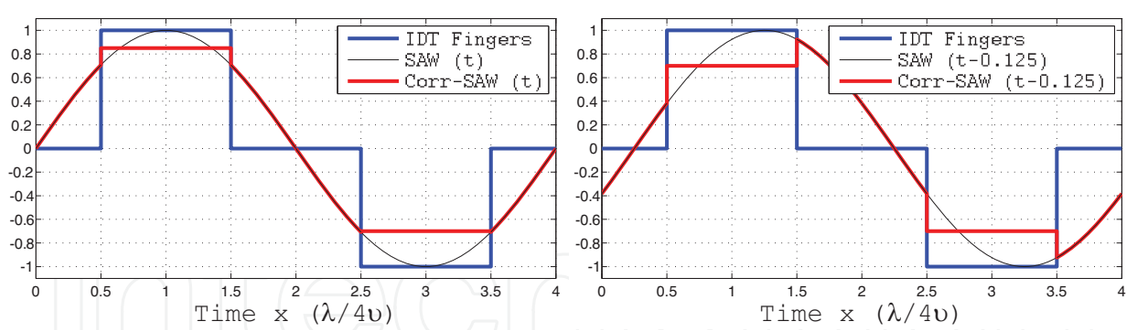

(a) time = t (b) time = $t - T/8$

Fig. 8. SAW correlation and the electric potential at the output IDT. Correlation between SAW electric potential and the output IDT of the SAW device is demonstrated. For a periodic IDT structure, one finger pair is represented, hence one time period ($T = \lambda/v$) is considered. Equipotential IDT fingers are represented by square waves. (a) Electric potential of the propagating SAW, $SAW(t)$ is peaked at the center of output IDT fingers (considered at time t). (b) Electric potential of the propagating SAW is $T/8$ seconds delayed compared to $SAW(t)$. In both the cases, the cross-correlated electric signal consists of equipotentials across IDT fingers.

6. Boundary condition analysis

As it was highlighted above, the weighting coefficients in Equations 16 and 17 need to be determined based on the electrical and mechanical boundary conditions applicable for the SAW device based actuator model. Therefore, in this section a detailed analysis is presented to determine these weighting coefficients.

Mechanical boundary conditions:

At the output IDT area of the SAW substrate, the IDT mass is taken to be negligible for simplicity, so that the mechanical force acting on the SAW substrate can be discarded. Hence the surface is considered to be mechanically free. This can be mathematically expressed as

$$\sum_j T_{3j} = 0, \tag{24}$$

where T is the mechanical stress tensor and j = 1, 2, 3.

Electrical boundary conditions:

In the SAW based electrostatic actuator model, the electric potential generated at the output IDT region was investigated and evaluated in Section 5. Based on Equation 23, at the surface where the output IDT is deposited (x_3 = 0), the electrical boundary condition constitute an electric potential at the IDT fingers, and the electric potential at the gaps between the IDT fingers. Respectively, these regions can be noted as ($0 \le x_1 \le \frac{\lambda}{4} \cup \frac{\lambda}{2} \le x_1 \le \frac{3\lambda}{4}$) and ($\frac{\lambda}{4} < x_1 < \frac{\lambda}{2} \cup \frac{3\lambda}{4} < x_1 < \lambda$) which correspond to Figure 6 for one period of the output IDT structure. As explained in Section 5, the electric potential wave at the output IDT fingers act as an equipotential time varying wave throughout the positive and negative IDT fingers (independent of x_1). Whereas the electric potential wave at the gap between the fingers, still a time varying and a moving wave (a function of x_1).

However, in the SAW device based actuator model (Figure 3), the conductive plate is placed at a height h above the output IDT, and connected to the common ground of the device. Therefore, the electric potential approaches zero at $x_3 = h$. It should be noted that the electric potential above the SAW substrate satisfies Laplace's equation, which results in an exponentially decaying electric signal in x_3 direction, and can be written as

$$\Phi_L(x_1, x_3, t) = \left[A_L e^{kx_3} + B_L e^{-kx_3} \right] e^{ik(x_1 - vt)}, \tag{25}$$

where A_L and B_L are constants. Additionally, the electric potential and the electric flux density in x_3 direction are continuous at the surface (x_3 = 0) (Subramanian et al., 1997; Maugin, 1985), which can be mathematically expressed as

$$\begin{aligned} \Phi(x_3 = 0^-) &= \Phi(x_3 = 0) = \Phi(x_3 = 0^+), \\ D(x_3 = 0^-) &= D(x_3 = 0) = D(x_3 = 0^+). \end{aligned} \tag{26}$$

Equation 23 along with conditions highlighted in Equation 26 are considered together to eliminate both A_L and B_L in Equation 25. First, the electrical boundary condition at the conductive plate is considered. Since the conductive plate mounted at a distance h above the substrate, the electric potential at $x_3 = h$ becomes zero. Therefore, from Equation 25,

$$\begin{aligned}\Phi_L(x_1,h,t) &= \left[A_L e^{kh} + B_L e^{-kh}\right] e^{\mathrm{i}k(x_1-vt)} = 0,\\ B_L &= -A_L e^{2kh}.\end{aligned} \tag{27}$$

Once B_L is eliminated, Equation 25 can be rewritten as,

$$\Phi_L(x_1,x_3,t) = A_L\left[e^{kx_3} - e^{2kh-kx_3}\right] e^{\mathrm{i}k(x_1-vt)}. \tag{28}$$

To evaluate the constant A_L, electrical boundary condition at the surface of the substrate ($x_3 = 0$) is need to be considered. However, as shown in Equation 23, the electric potential at the output IDT area is a combination of various potentials due to the output IDT and the gap between them. Therefore, two different electric potential signals have to be considered in the analysis, one considering the space above the output IDT ($0 \le x_1 \le \frac{\lambda}{4} \cup \frac{\lambda}{2} \le x_1 \le \frac{3\lambda}{4}$) and the other, the space above the output IDT gap ($\frac{\lambda}{4} < x_1 < \frac{\lambda}{2} \cup \frac{3\lambda}{4} < x_1 < \lambda$). More importantly, this distinction does not affect the final result due to the similarity in the procedure followed for the derivation of A_L. Therefore the approach is shown only for one case.

Considering the plane wave Equation 23 for electric potential and Equation 28, and the continuity Equation 26, A_L can be evaluated as follows,

$$\begin{aligned}\Phi_L(x_1,0,t) &= \Phi(x_1,0,t),\\ A_L\left[1-e^{2kh}\right].e^{\mathrm{i}k(x_1-vt)} &= \left[\sum_m \mathrm{C}_m \alpha_4^m\right].e^{\mathrm{i}k(x_1-vt)}, \text{ and}\\ A_L &= \frac{\sum_m \mathrm{C}_m \alpha_4^m}{\left[1-e^{2kh}\right]}.\end{aligned} \tag{29}$$

The relationship between the electric flux density and the electric field can be written as $D = \varepsilon_0 E$. Considering this relation along with Equation 1, a relationship between the electric flux density and the electric potential in the gap in x_3 direction can be written as

$$D_3(x_1,x_3,t) = -\varepsilon_0 \frac{\partial \Phi_L(x_1,x_3,t)}{\partial x_3}. \tag{30}$$

Hence, using the above equation, the electric flux density at $x_3 = 0$ is calculated and written as follows.

$$D_3(x_1,0,t) = -k\varepsilon_0 \frac{\sum_m C_m \alpha_4^m \left[1+e^{2kh}\right]}{\left[1-e^{2kh}\right]} e^{\mathrm{i}k(x_1-vt)}. \tag{31}$$

Additionally, another alternative expression for electric flux density at $x_3 = 0$ can be obtained from Equation 6. Therefore,

$$D_3(x_1,0,t) = \sum_j \sum_k e_{3jk} S_{jk} + \sum_j \varepsilon_{3j}^S E_j. \tag{32}$$

Ultimately, by equating Equations 31 and 32, another Eigenvalue problem is formulated, where the variables consist of the weighting coefficients. The resulting boundary conditions can be written out in matrix form as follows.

$$\begin{bmatrix} \mathbb{G} & 0 & \mathbb{H} & \mathbb{I} \\ \mathbb{J} & 0 & \mathbb{L} & \mathbb{N} \\ 0 & \mathbb{P} & 0 & 0 \\ \mathbb{Q} & 0 & \mathbb{R} & \mathbb{Y} \end{bmatrix} \begin{bmatrix} C_1 \\ C_2 \\ C_3 \\ C_4 \end{bmatrix} = 0, \tag{33}$$

where

$$\mathbb{G} = (c_{13} - c_{14}b^1)\alpha_1^1 + (-c_{14} + c_{11}b^1)\alpha_3^1 + (e_{13} - e_{22}b^1)\alpha_4^1$$
$$\mathbb{H} = (c_{13} - c_{14}b^3)\alpha_1^3 + (-c_{14} + c_{11}b^3)\alpha_3^3 + (e_{13} - e_{22}b^3)\alpha_4^3$$
$$\mathbb{I} = (c_{13} - c_{14}b^4)\alpha_1^4 + (-c_{14} + c_{11}b^4)\alpha_3^4 + (e_{13} - e_{22}b^4)\alpha_4^4$$
$$\mathbb{J} = c_{44}b^1\alpha_1^1 + (c_{44} - c_{14}b^1)\alpha_3^1 + e_{51}\alpha_4^1$$
$$\mathbb{L} = c_{44}b^3\alpha_1^3 + (c_{44} - c_{14}b^3)\alpha_3^3 + e_{51}\alpha_4^3$$
$$\mathbb{N} = c_{44}b^4\alpha_1^4 + (c_{44} - c_{14}b^4)\alpha_3^4 + e_{51}\alpha_4^4$$
$$\mathbb{P} = (c_{14} + c_{66}b^2)\alpha_2^2$$
$$\mathbb{Q} = e_{51}b^1\alpha_1^1 + (e_{51} + e_{22}b^1)\alpha_3^1 - (\varepsilon_{11}b^1 + \mathrm{i}\varepsilon_0\mathbb{X})\alpha_4^1$$
$$\mathbb{R} = e_{51}b^3\alpha_1^3 + (e_{51} + e_{22}b^3)\alpha_3^3 - (\varepsilon_{11}b^3 + \mathrm{i}\varepsilon_0\mathbb{X})\alpha_4^3$$
$$\mathbb{Y} = e_{51}b^4\alpha_1^4 + (e_{51} + e_{22}b^4)\alpha_3^4 - (\varepsilon_{11}b^4 + \mathrm{i}\varepsilon_0\mathbb{X})\alpha_4^4$$
$$\mathbb{X} = \frac{1 + e^{2hk}}{1 - e^{2hk}}.$$

Here the value of $\mathbb{X}$ depends on the position of the conductive plate above the SAW device (h), and takes the value of –1 for the case where the plate is at an infinite height above the substrate ($h \to \infty$). In this analysis, the phase velocity is explicitly present in Equations 16 and 17, and implicitly present in the roots b^m and in the linear coefficients α^m as mentioned before. Therefore a suitable value for phase velocity should be chosen for which the determinant of the coefficients in the Eigenvalue problem presented in Equation 33 vanishes, hence satisfy the associated boundary conditions.

It is important to realise that the above two Eigenvalue problems presented in Equations 15 and 33 are required to be solved simultaneously using iterative numerical procedures. This is due to the implicit dependency of decaying constants b^m on phase velocity v, and explicit dependency of Eigenvectors of linear coefficients α^m on v. Once a suitable phase velocity is found, the weighting coefficients C_m can be determined. As a result, a complete solution is obtained for the electric potential at the output IDT (Equation 23).

6.1 Electrostatic force generation

In electrostatic actuation, the electrostatic force applied on electrostatic plates can be described using the parallel plate capacitor effect (Tsai & Sue, 2007) as

$$F = \frac{1}{2}\frac{\varepsilon A \Phi^2}{(h - W_P)^2}, \tag{34}$$

where ε is the dielectric coefficient of the medium between the plates, A is the effective plate area, $W_P(x_1)$ is the instantaneous deflection of the actuator in x_3 direction, h is the initial plate spacing, and Φ is the applied electric potential between the plates.

In order to carry out the analysis to derive an expression for the resultant electrostatic force, the assumptions and simplifications mentioned in Section 4.2 are applied. Additionally, the electric field lines produced by the positive IDT fingers terminate either at the negative IDT fingers or at the conductive plate. For simplicity however, the effect of the electrostatic coupling between the IDT fingers, as well as the fringe capacitances (between the electrodes and the diaphragm), is discarded in this analysis.

Due to the periodic nature of the propagating waves and the placement of the IDTs, the electrostatic force analysis is initially carried out only for a single period, and then extended to the whole structure, similar to the electric potential calculation that is presented in Section 5. The single period placement of the output IDT is shown in Fig. 6.

Previously in Section 5, different segments of the output IDT were considered in analyzing the electric potential at output IDT. In this section, a similar approach is followed also in analysing the electrostatic force at the output IDT. Here, within one wavelength of the IDT, the analysis is carried out in two parts; one part considering the region above the output IDT electrodes ($0 \le x_1 \le \frac{\lambda}{4} \cup \frac{\lambda}{2} \le x_1 \le \frac{3\lambda}{4}$) and other, the region above the output IDT finger gaps ($\frac{\lambda}{4} < x_1 < \frac{\lambda}{2} \cup \frac{3\lambda}{4} < x_1 < \lambda$). This is due to the fact that was proven in Section 5; IDT fingers consisting of an equipotential distribution for a given time instance, while the gaps between the fingers consisting of a space varying electric potential distribution in x_1 direction as shown in Equation 23. In this analysis, an IDT with finger width of f_w and finger length of f_l is considered. For a metallisation ratio of 0.5 as in Fig. 6, the finger spacing is also f_w.

IDT Segment in Range ($0 \le x_1 \le \frac{\lambda}{4} \cup \frac{\lambda}{2} \le x_1 \le \frac{3\lambda}{4}$):

The electrostatic force generated by the electrode finger, which is connected to the positive bus bar $F_{(+)}$ can be evaluated considering Equations 23 and 34. As a result of the quadratic dependency of force to the applied electric potential, the force generated between the plate and the electrode finger, which is connected to the negative bus bar $F_{(-)}$ is equal to $F_{(+)}$. Therefore,

$$F_{(+)} = F_{(-)} = \frac{\varepsilon_0 f_l f_w}{2(h - W_P)^2}\left(\frac{2T}{\pi^2}\right)^2 \Phi^2\left(\frac{\lambda}{8}, x_3, t\right), \tag{35}$$

where ε_0 is the dielectric coefficient of air.

IDT Segment in Range ($\frac{\lambda}{4} < x_1 < \frac{\lambda}{2} \cup \frac{3\lambda}{4} < x_1 < \lambda$):

A slightly different approach is needed to evaluate the electrostatic force generated between the conductive plate and finger gaps. This is because of the space varying electric potential distribution mentioned above. Each finger gap is divided into N_s subdivisions in x_1 direction, so that each subdivision has a width of $\frac{f_w}{N_s}$ and a length of f_l (≈ aperture of the IDT). Combining the relevant range in Equations 23 and 34, and after some algebraic simplifications, the electrostatic force generated by each gap can be evaluated as

$$F_{(gap)} = \frac{\varepsilon_0 f_l f_w}{2N_s(h - W_P)^2} \cdot \left[\sum_j \Phi^2 (\frac{\lambda}{4} + \frac{j\lambda}{4N_s}, x_3, t) \right] \tag{36}$$

for j = 1, 2, 3,.., N_s. Therefore, for a distance of single wavelength (λ), the total electrostatic force generated is

$$F_{(\lambda)} = 2\left[F_{(+)} + F_{(gap)} \right]. \tag{37}$$

Furthermore, the above results can be used to extend the analysis to the evaluation of the resultant electrostatic force ($F_{(tot)}$) generated by an output IDT with N_p pairs of fingers. From Equations 35 – 37,

$$F_{(tot)} = \frac{C_t}{(h - W_P)^2} \sum_j \left[\left(\frac{2T}{\pi^2} \right)^2 \Phi^2 (\frac{\lambda}{8}, x_3, t) + \Phi^2 (\frac{\lambda}{4} + \frac{j\lambda}{4N_s}, x_3, t) \right] \tag{38}$$

for j = 1, 2, 3,.., N_s and $C_t = \frac{\varepsilon_0 f_l f_w N_p}{N_s}$.

As the doubly–clamped actuator is deflected due to the applied electrostatic force, an elastic restoring force is developed in the actuator. At equilibrium, the kinetic energy becomes zero, and actuator's potential energy reaches to a maximum. Therefore, to determine the displacement achieved by the actuator, the calculated electrostatic force and the elastic restoring force need to be considered at their equilibrium point (Washizu, 1975; Hu et al., 2004). However, this become a complex problem to solve since both the forces ($F_{(+)}$ and $F_{(gap)}$) depend on the actuator's instantaneous displacement $W_p(x_1)$. Therefore, to obtain an accurate solution for $W_P(x_1)$, analytical methods or numerical analysis methods such as FEM are required.

7. Finite element modelling of the actuator

For the Finite Element Analysis (FEA) of the actuator, a coupled–filed analysis is required since electrostatic and solid interactions are involved. Two distinct coupled–field methods can be identified in ANSYS; (i) Direct-coupling method, and (ii) Load transfer method (ANSYS Incorporation, 2009).

The direct–coupling method involves just one analysis that uses a coupled–field element type containing all necessary degrees of freedom. The coupling is handled by calculating element matrices or element load vectors that contain all necessary terms. Whereas the load transfer methods involve two or more analysis with each belonging to a different field, and two fields are coupled by applying results from one analysis as loads in another analysis.

There are different types of load transfer analysis in ANSYS; (i) ANSYS Multi–field Solver (MFS and MFX), (ii) Physics file based load transfer, and (iii) Unidirectional load transfer (ANSYS Incorporation, 2009). Suitability of these methods for a certain analysis depends on the physics fields involved, and whether the load transfer is unidirectional or not. Therefore, it is crucial to chose the most appropriate method to analyse a given scenario in order to achieve more accurate results in a reasonable simulating time. However, for MEMS applications ANSYS Multi–field solver is highly appropriate as it is a solver for sequentially coupled field analysis. Therefore in this research, ANSYS MFS is used for FEA of the SAW device based actuator.

7.1 Preparation of the model for analysis

The steps that were followed in the design and modelling of this device is as follows. Initially the geometry is created, and then element and material properties are defined for the actuator and the air–gap. As depicted in Figure 9, SOLID95 and SOLID122 element types are used for the structural and electrostatic models respectively. SOLID95 element has capabilities such as plasticity, creep, stress stiffening, large deflection, and large strain capability hence highly suitable for the design of microactuators. Whereas, SOLID122 is a 3D, 20–node, charge based electric element, which has one degree of freedom (Voltage) at each node. It is designed to tolerate irregular shapes without much loss of accuracy. Moreover, SOLID122 elements have compatible voltage shapes and are well suited to model curved boundaries and applicable to 3D electrostatic and time–harmonic, quasi–static electric field analysis (ANSYS Incorporation, 2009). In this modelling, the effect of the output IDT is designed by coupling a set of nodes at the bottom of the air–gap to match the desired IDT pattern and assigning a Volt Degree–of– Freedom (DoF) to those nodes.

Next, the geometry is meshed to a fine level to accommodate for accurate micro level changes in the structure. Once the geometry is meshed, relevant electric and mechanical boundary conditions are applied. After setting the boundary conditions and constrains, a static analysis is carried out mainly to check for the convergence criteria. Once the results are converged in static analysis, then a model analysis is carried out to extract the natural frequencies of the conductive actuator. As a result, the operating mode for the actuator can be realised, and then a transient analysis is performed for a long enough time period that is dictated by the natural frequency mode of the actuator and the frequency of operation of the SAW device. This is an important step in the modelling process as it helps to decide on an optimal completion time for the transient analysis, since the transient simulations generally take a longer time to complete.

To simplify the analysis, the performance of the thin conductive plate with a smaller width was initially considered. Additionally, half–symmetry is exploited due to the symmetrical nature of the model. As a result, a reduced number of nodes and elements were generated for the model, and hence reduced simulation times and improved CPU usage were achieved.

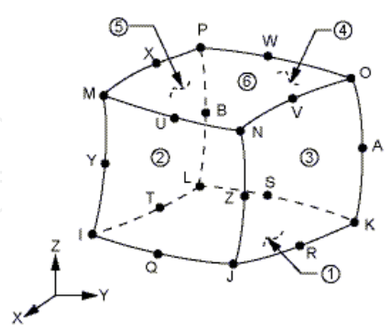

Fig. 9. SOLID95 and SOLID122 element geometries. 3D, 20–node elements used in the design of actuator and the air–gap (ANSYS Incorporation, 2009). SOLID95 element has capabilities such as plasticity, creep, stress stiffening, large deflection, and large strain capability. SOLID122 is a charge based electric element with one degree of freedom (Voltage) at each node. SOLID122 elements are well suited to model curved boundaries and applicable to 3D electrostatic and time–harmonic quasi–static electric field analysis (ANSYS Incorporation, 2009).

8. Simulations and results

8.1 Static analysis

Initially, the static analysis was carried out to determine the static displacement of the actuator. In order to mimic the effect of the electric potential wave generated at the output IDT of the SAW device, a set of interleaved electrodes were used and every alternative electrode was coupled, so that one set of electrodes act as the positive bus bar and the other as the negative bus bar. Hence, in the microactuator modelling, the whole SAW device was replaced at simulation level. Material properties of silicon were used for the doubly–clamped conductive plate, which in turn acts as a microactuator. The conductive plate dimensions were chosen to be 1000 μm × 2 μm × 10 μm ($L \times H \times W$). The gap between the electrodes and the conductive plate h was taken to be 10 μm and was considered to be filled with air. For static analysis, a 10 Volt input voltage was applied to the positive bus bar. The negative bus bar and the conductive plate was connected to a common ground to form the electrostatic field.

Initial FEA results are verified using a commonly used Rayleigh–Ritz method based analytical model. For comparison purposes, displacement versus voltage results were plotted and are shown in Figure 10. A good correlation can be observed between the analytical and simulation results for the microactuator. However, FEA results demonstrate slightly lower displacements for a given voltage. This is mainly because the full thickness of the actuator was considered in the simulated 3D model in FEA, whereas the actuator was modeled as a thin plate in the Rayleigh–Ritz method based analytical model. Therefore, the higher bending stiffness reduces the effective mid–beam displacement in the FEA model. It should be noted that the actuator displacement can be increased by reducing the gap between the conductive plate and the output IDT, reducing the thickness of the conductive plate, and reducing the stress level applied at the actuator by optimising the clamping mechanism.

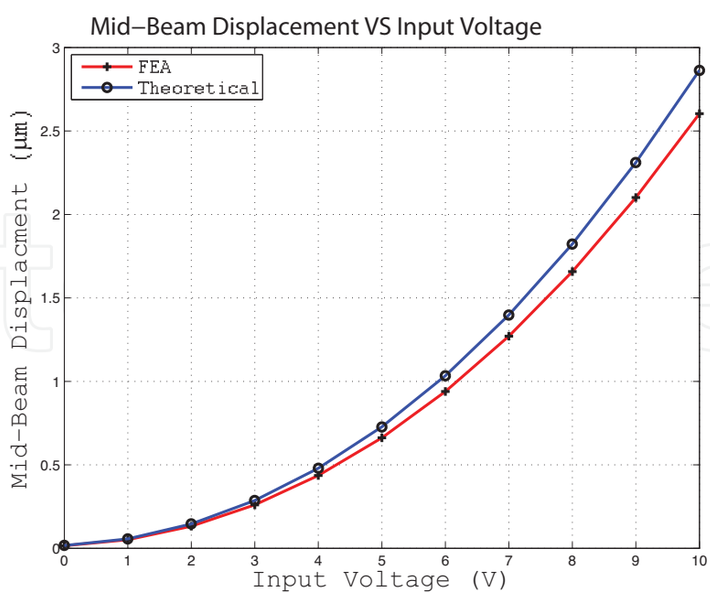

Fig. 10. Simulation and theoretical results. Comparison of simulated and theoretical results for the SAW actuator. Displacement VS Voltage plot for the mid-beam displacement in the conductive plate actuator above the SAW device.

Once the static analysis was completed more detailed transient analyses were performed in ANSYS to investigate the dynamic behavior of the actuator.

8.2 Transient analysis

It should be noted that when a conductive beam is subject to a dynamically changing electrostatic field, the displacement behaviour needs to be calculated analytically or numerically; using advanced simulation tools equipped with in built algorithms, such as ANSYS. This section presents the transient simulation results carried out for the conductive plate with the same dimensions mentioned in the static analysis above. Moreover, an AC sinusoidal wave with a frequency of 50 MHz and a peak voltage of 10 volts were used to emulate the electric potential wave at the output IDT as proven in Equation 23. The conductive plate is connected to ground so that the plate acts as an equipotential surface. However, the node density of the model, and the CPU processing power were found to be major constrains that restricted longer transient analysis (ex: 1000×T, where T is the period of SAW). Moreover, a higher node density was needed to effectively represent the output IDT in FEA model. By considering these factors, transient simulations were performed for 400×T during this analysis.

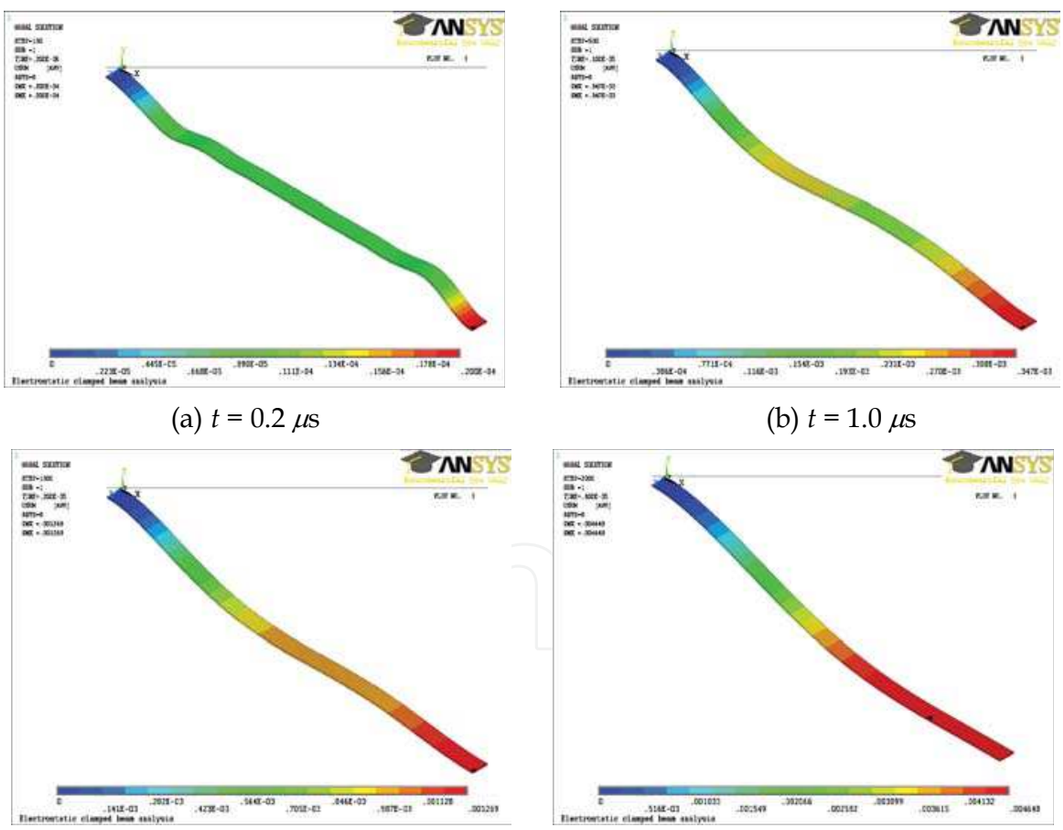

(a) t = 0.2 μs (b) t = 1.0 μs

(c) t = 2.0 μs (d) t = 4.0 μs

Fig. 11. Transient analysis results for intermediate steps. Deflection results for the actuator performance at various time steps during the transient analysis. Half–symmetry is exploited due to the symmetrical nature of the model. The flexural behaviour is observed during stabilisation period.

Figures 11 – 12 depict the actuator displacements for different steps in transient analysis. As a thinner actuator is modelled in ANSYS, the flexural behavior of the actuator is first observed. As the time progresses, the deflection profile of the actuator is found to be similar to the profile obtained from the Rayleigh–Ritz method based analysis.

Figures 12 (c) and (d) depict the contour plot of the Von Mises stress distribution of the actuator. Here, Von Mises stress can be used to predict the yielding of any of the materials used, under any loading condition. The maximum Von Mises stress in this scenario is 0.121 MPa, which is much lower than the yield strengths of the selected material. This demonstrates that the actuator's deflection is well within the elastic range of the materials used.

As can be seen from these simulations, micro displacements are successfully obtained using SAW based actuation method. Figure 13 shows the mid–beam and the quarter–beam displacement variations over a simulation time of 400×T. Based on the static analysis however, it was shown that displacements up to ~3 μm can be achieved using SAW device

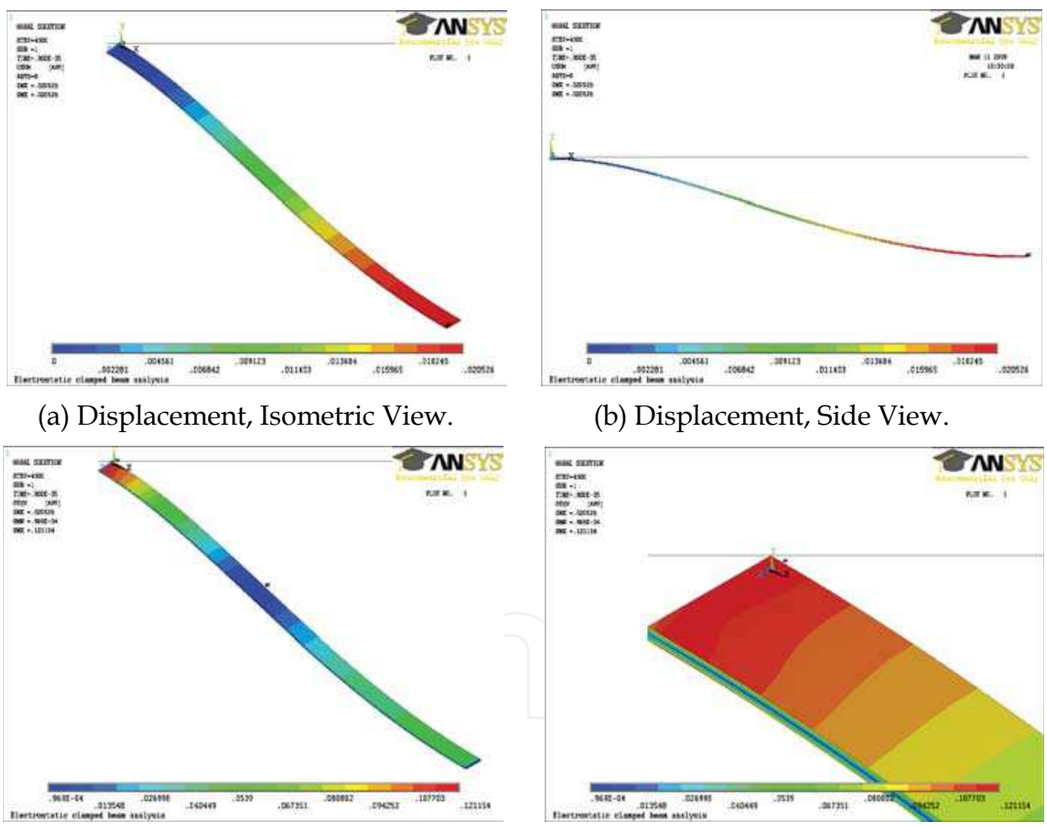

(a) Displacement, Isometric View. (b) Displacement, Side View.

(c) Von Mises stress, Isometric View. (d) Von Mises stress, Clamped edge.

Fig. 12. Transient analysis results for final step. Deflection and Von Mises stress analysis results for the actuator performance at t = 8.0 μs. Half–symmetry is exploited due to the symmetrical nature of the model. The maximum Von Mises stress in this scenario is 0.121 MPa, which is near the clamped edge. This is much lower than the yield strengths of the selected material, hence demonstrating that the actuator's deflection is well within the elastic range.

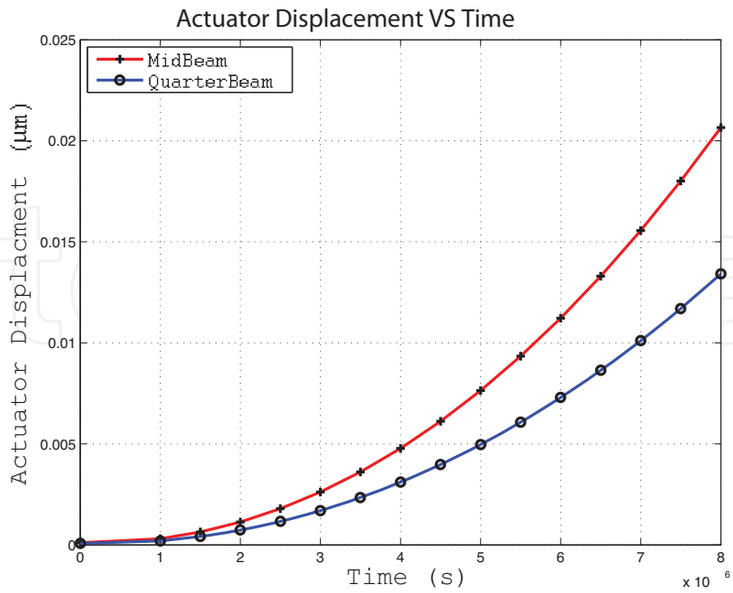

Fig. 13. Displacement VS Time plot of the mid–beam. Analysis carried out for 400×*T*, where *T* is the time period of the SAW signal. As the time increases the mid–beam displacement as well as the quarter–beam deflection increase at an increasing rate.

based actuation. As a result, it is proven that even after 400×*T*, still the dynamic displacement does not show any periodic nature but in the process of gaining more displacement. Based on these results, it is evident that the actual operating frequency of the conductive plate during actuation is a very much a scaled down version of the SAW frequency.

9. Conclusion

In this chapter, the use of a SAW device to generate microactuations was demonstrated. Detailed theoretical analysis explaining how the entire SAW device based actuator operation was carried out and boundary conditions applicable for presented design was used to derive the electric potential wave forms, hence the electrostatic field between the SAW device and the conductive plate. Displacement analysis of the conductive actuator was obtained. Static analysis results were generated using the ANSYS simulation tool, and compared with the theoretical results obtained by Rayleigh–Ritz method. A good correlation between the theoretical and simulated displacement curves were observed.

Once the static analysis was completed, the dynamic behaviour of the SAW device based electrostatic actuator was studied using transient analysis. This is more substantial in investigating the operating frequency of the conductive plate. Since the SAW frequency is in the range between 50 MHz–1 GHz it was crucial to verify the effective operating frequency of the conductive plate. Because of the time varying electrostatic field, it was found that the oscillating frequency of the actuator is much less than that of the SAW frequency. Therefore, the applicability of this SAW based secure and wireless interrogation for implantable MEMS devices is clearly demonstrated.

10. References

Adler, E. L. (2000). Bulk and surface acoustic waves in anisotropic solids, *International Journal of High Speed Electronics and Systems* 10(3): 653–684.

ANSYS Incorporation (2009). ANSYS Help Guide–V.11. *http://www.kxcad.net/ansys/ANSYS/ansyshelp/ index.htm* (visited on 25/05/2010).

Dissanayake, D.W., Tikka, A. C., Al-Sarawi, S. &Abbott, D. (2007). Radio frequency controlled microvalve for biomedical applications, *Proc. of SPIE–Smart Materials IV* 6413: Article 64130D: 1–13.

Dvoesherstov, M. Y. & Chirimanov, A. P. (1999). Numerical analysis of a surface and leaky surface acoustic wave in new piezoelectric $KNbO_3$, PKN, and LGN crystals, *Radiophysics and Quantum Electronics* 42(5): 431–438.

Dvoesherstov, M. Y., Petrov, S. G., Cherednik, V. I., & Chirimanov, A. P. (2000). Transformation of modes of surface acoustic waves in strong $KNbO_3$ and PKN piezoelectric crystals, *Radiophysics and Quantum Electronics* 43(5): 400–406.

Gantner, A., Hoppe, R. H.W., Köster, D., Siebert, K. G. & Wixforth, A. (2007). Numerical simulation of piezoelectrically agitated surface acoustic waves on microfluidic biochips, *Computing and Visualization in Science* 10(3): 145–161.

Gardner, J. W., Varadan, V. K. & Awadelkarim, O. O. (2001). *Microsensors, MEMS, and Smart Devices*, First edn, Tsinghua University Press, Beijing, chapter : Microsensors, Introduction to SAW devices, Surface acoustic waves in solids, IDT microsensor parameter measurement, IDT microsensor fabrication, IDT microsensors, pp. 227–396.

Horenstein, M. N., Perreault, J. A. & Bifano, T. G. (2000). Differential capacitive position sensor for planar MEMS structures with vertical motion, *Sensors and Actuators* 80: 53–61.

Hu, Y. C., Chang, C. M. & Huang, S. C. (2004). Some design considerations on the electrostatically actuated microstructures, *Sensors and Actuators A* 112: 155–161.

Ippolito, S. J., Kalantar-zadeh, K., Wlodarski, W. & Powell, D. A. (2002). Finite-element analysis for simulation of layered SAWdevices with XY LiNbO3 substrate, *Proc. of SPIE– Smart Structures, Devices, and Systems* 4935: 120–131.

Jones, I., Ricciardi, L., Hall, L., Hansen, H., Varadan, V., Bertram, C., Maddocks, S., Enderling, S., Saint, D., Al-Sarawi, S. & Abbott, D. (2008). Wireless RF communication in biomedical applications, *Smart Materials and Structures* 17: 015050: 1–10.

Kannan, T. (2006). *Finite element analysis of surface acoustic wave resonators*, Master's thesis, University of Saskatchewan.

Maugin, G. A. (1985). *Nonlinear electromachanical effects and applications*, First edn,World Sceintific Publishing Co. Pte. Ltd., chapter : Rayleigh Surface Waves, pp. 104–142.

Milstein, L. B. & Das, P. (1979). Surface AcousticWave Devices, *IEEE Communications Magazine* 17: 25–33.

Ruppel, C. C. W., Reindl, L. & Weigel, R. (2002). SAW devices and their wireless communication applications, *IEEE Microwave Magazine, ISSN 1527-3342* 3(2): 65–71.

Skinner, J. L., Cardinale, G. F., Talin, A. A. & Brocato, R.W. (2006). Effect of critical dimension variation on SAWcorrelator energy, *IEEE Transactions on Ultrasonics, Ferroelectrics and Frequency Control* 53(2): 497–501.

Strobl, C. J., Guttenberg, Z. V. & Wixforth, A. (2004). A Nano–and pico–dispensing of fluids on planar substrates using SAW, *IEEE Transactions on Ultrasonics, Ferroelectrics, and Frequency Control* 51(11): 1432–1436.

Subramanian, H., Varadan, V. K., Varadan, V. V. & Vellekoopz, M. J. (1997). Design and fabrication of wireless remotely readable MEMS based microaccelerometers, *Smart Materials and Structures* 6(6): 730–738.

Tsai, N. C. & Sue, C. Y. (2007). Review of MEMS–based drug delivery and dosing systems, *Sensors and Actuators A* 134: 555–564.

Upadhyay, S. K. (2004). *Seismic Reflection Processing: With Special Reference to Anisotropy*, First edn, Springer–Verlag, Berlin, chapter: Anisotropy Models of Sedimentary Sections and Characteristics of Wave Propagation, pp. 143–201.

Varadan, V. K. & Varadan, V. V. (2000). Microsensors, micromechanical systems (MEMS), and electronics for smart structures and systems, *Smart Materials and Structures* 9: 953–972.

Čiplys, D. & Rimeika, R. (1999). Measurements of electromechanical coupling coefficient for surface acoustic waves in proton-exchanged lithium niobate, *ULTRAGARSAS journal* 33(3): 14–20.

Washizu, K. (1975). *Variational methods in elasticity and plasticity*, Second edn, Pergamon Press Ltd., Oxford, chapter : Beams, Plates, pp. 132–182.

Wixforth, A. (2003). Acoustically driven planar microfluidics, *Superlattices and Microstructures* 6: 389–396.

Wolfram MathWorld (2009). Euler angles. *http://mathworld.wolfram.com/EulerAngles.html* (visited on 25/05/2010).

Zaglmayr, S., Sch¨berl, J. & Langer, U. (2005). *Progress in Industrial Mathematics at ECMI 2004*, Vol. 8 of *Mathematics in Industry*, Springer–Verlag, Berlin, chapter: Eigenvalue Problems in Surface Acoustic Wave Filter Simulations, pp. 75–99.

Acoustic Waves

Edited by Don Dissanayake

ISBN 978-953-307-111-4

Hard cover, 434 pages

Publisher Sciyo

Published online 28, September, 2010

Published in print edition September, 2010

SAW devices are widely used in multitude of device concepts mainly in MEMS and communication electronics. As such, SAW based micro sensors, actuators and communication electronic devices are well known applications of SAW technology. For example, SAW based passive micro sensors are capable of measuring physical properties such as temperature, pressure, variation in chemical properties, and SAW based communication devices perform a range of signal processing functions, such as delay lines, filters, resonators, pulse compressors, and convolvers. In recent decades, SAW based low-powered actuators and microfluidic devices have significantly added a new dimension to SAW technology. This book consists of 20 exciting chapters composed by researchers and engineers active in the field of SAW technology, biomedical and other related engineering disciplines. The topics range from basic SAW theory, materials and phenomena to advanced applications such as sensors actuators, and communication systems. As such, in addition to theoretical analysis and numerical modelling such as Finite Element Modelling (FEM) and Finite Difference Methods (FDM) of SAW devices, SAW based actuators and micro motors, and SAW based micro sensors are some of the exciting applications presented in this book. This collection of up-to-date information and research outcomes on SAW technology will be of great interest, not only to all those working in SAW based technology, but also to many more who stand to benefit from an insight into the rich opportunities that this technology has to offer, especially to develop advanced, low-powered biomedical implants and passive communication devices.

How to reference

In order to correctly reference this scholarly work, feel free to copy and paste the following:

Don Dissanayake, Said Al-Sarawi and Derek Abbott (2010). Surface Acoustic Wave Based Wireless MEMS Actuators for Biomedical Applications, Acoustic Waves, Don Dissanayake (Ed.), ISBN: 978-953-307-111-4, InTech, Available from: http://www.intechopen.com/books/acoustic-waves/surface-acoustic-wave-based-wireless-mems-actuators-for-biomedical-applications

INTECH
open science | open minds

InTech Europe
University Campus STeP Ri
Slavka Krautzeka 83/A
51000 Rijeka, Croatia

InTech China
Unit 405, Office Block, Hotel Equatorial Shanghai
No.65, Yan An Road (West), Shanghai, 200040, China
中国上海市延安西路65号上海国际贵都大饭店办公楼405单元

Phone: +385 (51) 770 447
Fax: +385 (51) 686 166
www.intechopen.com

Phone: +86-21-62489820
Fax: +86-21-62489821

IntechOpen

IntechOpen

© 2010 The Author(s). Licensee IntechOpen. This chapter is distributed under the terms of the Creative Commons Attribution-NonCommercial-ShareAlike-3.0 License, which permits use, distribution and reproduction for non-commercial purposes, provided the original is properly cited and derivative works building on this content are distributed under the same license.